DOI: 10.1111/cgf.14318
Eurographics Conference on Visualization (EuroVis) 2021
R. Borgo, G. E. Marai, and T. von Landesberger
(Guest Editors)

Volume 40 (2021), Number 3

Implicit Modeling of Patient-Specific Aortic Dissections with Elliptic Fourier Descriptors

G. Mistelbauer[1], C. Rössl[1], K. Bäumler[2], B. Preim[1], and D. Fleischmann[2]

[1]Department of Simulation and Graphics, Otto-von-Guericke University Magdeburg, Germany
[2]3D and Quantitative Imaging Laboratory, Department of Radiology, Stanford University School of Medicine, Stanford, CA, USA

Abstract

Aortic dissection is a life-threatening vascular disease characterized by abrupt formation of a new flow channel (false lumen) within the aortic wall. Survivors of the acute phase remain at high risk for late complications, such as aneurysm formation, rupture, and death. Morphologic features of aortic dissection determine not only treatment strategies in the acute phase (surgical vs. endovascular vs. medical), but also modulate the hemodynamics in the false lumen, ultimately responsible for late complications. Accurate description of the true and false lumen, any communications across the dissection membrane separating the two lumina, and blood supply from each lumen to aortic branch vessels is critical for risk prediction. Patient-specific surface representations are also a prerequisite for hemodynamic simulations, but currently require time-consuming manual segmentation of CT data. We present an aortic dissection cross-sectional model that captures the varying aortic anatomy, allowing for reliable measurements and creation of high-quality surface representations. In contrast to the traditional spline-based cross-sectional model, we employ elliptic Fourier descriptors, which allows users to control the accuracy of the cross-sectional contour of a flow channel. We demonstrate (i) how our approach can solve the requirements for generating surface and wall representations of the flow channels, (ii) how any number of communications between flow channels can be specified in a consistent manner, and (iii) how well branches connected to the respective flow channels are handled. Finally, we discuss how our approach is a step forward to an automated generation of surface models for aortic dissections from raw 3D imaging segmentation masks.

CCS Concepts

• ***Human-centered computing*** → ***Scientific visualization;*** • ***Applied computing*** → ***Health informatics;*** • ***Computing methodologies*** → ***Parametric curve and surface models;***

1. Introduction

Aortic dissection (AD) is a rare but life-threatening vascular disease [WFEG*20] that is pathologically characterized by a semi-circumferential delamination of the aortic media layer. This leads to formation of a new flow channel—the false lumen—within the thinned, delaminated wall, that is separated from the original channel—the true lumen—by a membrane, the so-called dissection flap [MHM*16]. Patients with dissection of the ascending aorta—type A aortic dissection (TAAD)—require urgent surgical repair [CM16]. If the ascending aorta is not involved—type B aortic dissection (TBAD)—endovascular aortic repair is indicated if acute complications occur, such as aortic rupture, and branch vessel malperfusion (complicated TBAD). Patients without complications can be managed medically (uncomplicated TBAD) [HBB*10]. All survivors of acute AD remain at high risk of late complications, predominantly driven by false lumen degeneration and aneurysm formation, and require lifelong surveillance and imaging. Once the aorta reaches 5.5 cm in diameter, elective surgical repair is indicated to prevent rupture.

There is growing evidence that morphologic features of aortic dissection predict aneurysm formation and late complications. The morphologic features of interest include the geometry and relative arrangement of the true and false lumen, the communications between them across the dissection flap, and the specific arrangement of aortic branch vessels relative to both lumina. More branches arising off the false lumen improves drainage and putatively lowers the false lumen pressure. A prediction model based on four manually extracted morphologic dissection features was able to discriminate between high-risk and other patients with uncomplicated TBAD [SvKN*17]. A more refined patient-specific approach to estimate the pressure within the false lumen—which is the ultimate driving force for late complications—requires detailed modeling.

Bäumler et al. [BVS*20] recently presented a numerical model to simulate hemodynamics and pressures in patient-specific models of aortic dissection, using fluid-structure interactions. This approach requires 3D models of both the vessel lumen (fluid domain) and the vessel wall (structural domain). They showed how the dissection flap elasticity can affect true and false lumen pressures and flow rates. However, reliable measurement of imaging features and automatic

generation of 3D models for hemodynamic simulations require an aortic model that can capture the varying anatomy of ADs.

Three-dimensional surface representations of vascular structures can be created explicitly with truncated cones [HPSP01], point-cloud polygonization [WWL*10] or implicitly using Gaussians [OP05], multi-level partition of unity implicits [SOB*07], or extrusion surfaces [KGPS13, HLW*18]. The majority of explicit and implicit model-based approaches either support only circular cross-sections [HPSP01, OP05] or use spline-based representations [KGPS13, HLW*18], but present mainly convex shapes.

In this work, we present a model-based approach for the representation of AD surfaces based on elliptic Fourier descriptors (EFDs) of a chain-coded flow channel's cross-sectional contour [KG82]. The EFD representation of contours on each 2D image slice allows us to

- control the smoothness of a cross-sectional contour by gradually removing high-frequency details while retaining the overall shape,
- model concave cross-sections separated by a dissection flap,
- model the outer vessel wall with a lumen-specific thickness, and
- create an abstraction of the dissected aorta.

Rendering EFDs into a 3D model is then governed by smoothly blending the cross-sections into the final surface representation.

2. Related Work

This work focuses on the cross-sectional representation of vessel contours in ADs via EFDs. Related work includes 2D contour representations such as chain codes and Fourier descriptors (FDs). Since individual cross-sections are then combined into a single surface representation, we also discuss relevant work in that field.

2.1. Chain Codes

Chain codes represent discrete contours by encoding the directions of movement along the contour, instead of storing the spatial positions. These directions are determined either absolutely in relation to its enclosing reference system (image or volume) or relative to the current orientation, with the latter referred to as differential chain code (DCC). Absolute chain codes are invariant under translation, but not rotation, while DCCs are also rotationally invariant. Chain codes are easy to compare, but sensitive to noise. This sensitivity can be handled by creating them at a coarser resolution [YKR08].

One of the most prominent chain codes is the Freeman chain code (FCC) [Fre61]. It constitutes a compact representation of a 2D discrete contour by using the numbers 0-3 (4-connected) or 0-7 (8-connected) on a rectangular lattice. The vertex chain code (VCC), proposed by Bribiesca [Bri99], follows the vertices around pixels, i.e., the VCC of a single pixel is `1111` (its four edges), compared to its FCC of `0`. When dealing with a DCC, such as the VCC, the reconstruction of a shape's contour requires finding a rotationally invariant start position, transforming the code into slope changes, and integrating these along the code. Liu and Žalik [LŽ05] proposed a more compact FCC-based relative chain code by encoding the forward direction as zero and the other directions as Huffman code (with a trailing zero, or at most 7 bits long). Sánchez-Cruz et al. [SCBRD07] assessed the compression efficiency of chain codes.

The FCC can also describe discrete 3D curves on cubic lattices [Fre74]. Bribiesca [Bri00] presented a relative 3D chain code based on the directional changes of a polyline. Encoding the changes of a 3D contour only in right (0) and left (1) leads to a binary code [Bri04]. Trees, as described by Bribiesca [Bri08], can also be expressed by a relative chain code, where a single chain element can take any number between 0-4 and branches are modeled with parentheses. Sánchez-Cruz et al. [SCLVC14] presented another relative chain code for 3D curved trees. The code comprises 72 different directional changes, divided into three groups of 24 directions each and coded with a single alphabetical letter. Strnad et al. [SKNŽ20] proposed a compressed chain code for 3D tree structures that allows building different levels-of-detail (LoDs).

2.2. Fourier Descriptors

Fourier descriptors (FDs) can be used to describe and analyze shapes according to similarity, symmetry, and mirroring. For example, they are used in biology [IU02] to differentiate grain types [MPJ12], plant leaves [CO17], or rice grain [IEUH15]. A comprehensive overview of object or shape descriptors is given by Nixon and Aguado [NA02] and Yang et al. [YKR08].

Fourier descriptors (FDs) were employed by Zahn and Roskies [ZR72] for closed planar contours of 2D shapes. The contours are arc-length parametrized and mapped to a periodic function of period 2π. These functions are then expanded as a Fourier series, whose coefficients comprise the FDs, which consist of pairs of harmonic amplitude and phase angle. By FCC-coding discrete 2D contours, their shape can be expressed as the loci of several connected ellipses, leading to elliptic Fourier descriptors (EFDs) [KG82]. The authors describe several EFD-based features for discriminating shapes and how to normalize EFDs to be independent of starting point location, translation, and size. Lin and Hwang [LH87] proposed orientation- and translation-independent invariants for EFD-based shape characterization. They also mention that a shape is usually characterized by lower order harmonics and that three to six harmonics might be sufficient. This is one of the motivations for modeling vessel cross-sections with EFDs, since their LoD can be controlled and adapted to specific applications. Aguado et al. [AMZ99] describe a generalized cylinder as a sweep surface along a trajectory with different top and bottom cross-sections expressed by EFDs. Intermediate cross-sections are interpolated in the Fourier domain. To perform a meaningful interpolation, a suitable point correspondence between the two modeled cross-sections is necessary. This can be done either with arc-length parametrization or based on landmarks. The (axial) reslicing of shapes by interpolation of EFD coefficients was discussed by Jeong and Radke [JR07] with respect to different organs, such as prostate, bladder or kidney. By resampling the resulting contours at equal angles from the center of the shape, successive slices have the same number of contour points. Finding suitable point correspondences in ADs might be difficult, because the lumina can be concave and revolve around each other. Sato et al. [SIK*17] investigated EFDs as an effective predictor of aortic enlargement in TBAD. They calculated 20 harmonics of the true lumen and performed a principal component analysis to evaluate the variation of the coefficients.

2.3. Vessel Modeling

Vascular surface modeling can be categorized into model-based vs. model-free and implicit vs. explicit. Model-based approaches assume a cross-section model, e.g., circular or elliptical, whereas model-free methods extract a surface, e.g., from point clouds. For a comprehensive overview, the reader is referred to [HLW*20].

Explicit methods usually create the vessel surface either directly from a centerline by connecting the vertices of consecutive cross-sections [HPSP01] (explicit model-based) or from point clouds [WWL*10] (explicit model-free). Common difficulties of explicit vascular modeling are highly curved regions and branches [HLT12]. Implicit algorithms are based on implicit functions or distance-fields and produce smooth surfaces. Implicit model-free approaches usually fit a surface to a point-cloud [SOB*07, QLCH20] and then reconstruct the surface using iso-surface extraction. Since our work belongs to the implicit model-based approaches, we subsequently discuss the relevant works in detail, but focus on their cross-sectional representations.

Li and Tian [LT09] introduced piecewise algebraic (PA) splines for modeling freeform 2D implicit curves. Their explicit form allows fast evaluation with a controlled degree of smoothness with respect to the initial polygon. A suitable smoothness may depend on the target application and the desired degree of interpolation. Later, Li and Tian [LT11] proposed partial shape-preserving (PSP) splines for a given control polygon as the composition of primitive basis functions, such as the piecewise polynomial smooth unit step function [LGW06, Li07]. Like PA splines, PSP splines provide control over blending strength, but limit the blending to a certain range. This is particularly useful when blending vascular cross-sections, as done by Hong et al. [HLT12]. They implicitly model generalized cylinders [AMZ99] with PA splines and blend them longitudinally with PSP splines. Kretschmer et al. [KGPS13] used spline-based cross-sections for implicit vascular modeling of high-quality meshes even at furcations. Undesired sharp blending and bulging are avoided by employing a gradient-based blending operation [GBC*13]. Smooth blending of 2D cross-sections can be achieved either by weighted blending [HLW*18] or by interpolating between a reduced number of cross-sections [KGPS13]. Undesirable deviations, e.g. caused by noise or segmentation artifacts, between successive cross-sections can be reduced by constraining their shape, e.g., to an ellipse [KGPS13, HLW*18]. Hong et al. [HLW*18] used ellipse-constrained radial basis functions [LWP*04] to model vascular cross-sections and PSP splines for blending. Eigen et al. [EWD*18] segmented the inner and outer vessel wall of ADs with active contour models and used compactly supported radial basis functions for surface reconstruction. In comparison, we consider the aorta with its branches and propose a model for both lumina and the outer vessel wall. Hong et al. [HLW*20] subdivided the centerline of a vessel branch into segments and modeled them as intersection of orthogonal implicit functions. Cross-sections are modeled by a polynomial curve fit to local contour points. Abdellah et al. [AGL*20] rendered large vascular networks based on metaballs.

In summary, implicit model-based approaches mainly describe cross-sections with splines or radial basis functions, optionally constrained by ellipses. We subsequently describe the implicit generation of smooth surfaces with cross-sections modeled by EFDs.

3. Methods

Motivated by the ultimate goal to create surface representations of ADs directly from 3D segmentation masks that are suitable for computational fluid dynamics (CFD) simulations [BVS*20], we propose the following workflow (see Fig. 1): *(a)* create a vessel tree that represents the AD and its multiple lumina well, *(b)* extract and reconstruct the inner, luminal contours of each flow channel as well as the common outer vessel wall, and *(c)* combine the individual cross-sections into branches and smoothly blend these together to form the final lumen and wall surfaces. In the subsequent sections, we describe each step of our workflow in detail.

3.1. Vessel Tree Extraction

As input, we start with the 3D segmentation mask of the aorta and some of its branches, mainly including the arteries of the arch and the abdominal aorta [MSS*16]. This mask consists of background, true lumen, and optionally, if existing, false lumen.

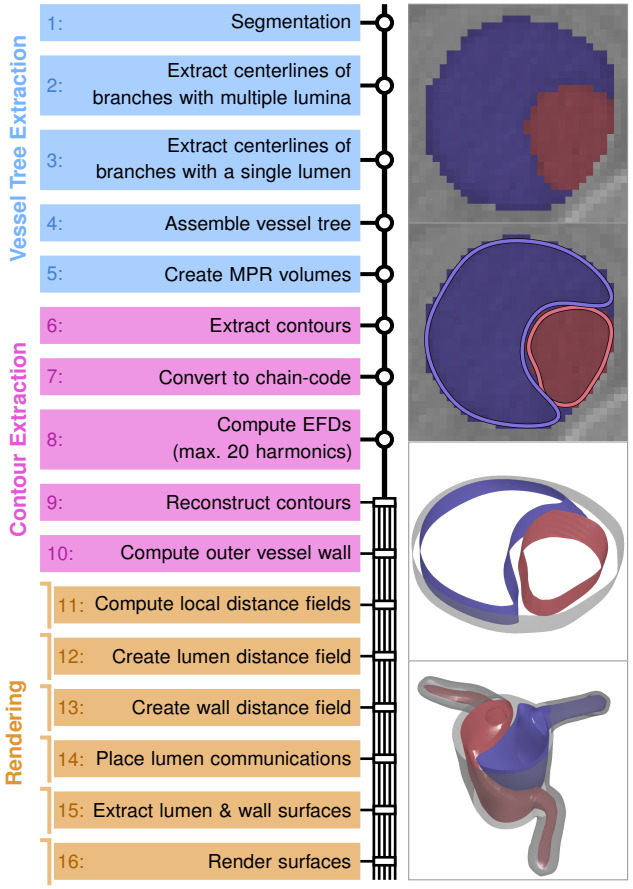

Figure 1: *Workflow of our proposed approach. The steps connected with a single line (1-8) are only computed once per data set, whereas the steps connected with multiple lines (9-16) are computed whenever the number of harmonics, the number of reconstructed contour points, or the thickness of the vessel wall is changed. All rendering steps use OpenGL compute shaders, indicated by the GPU icon, while the other parallel steps are executed on the CPU using OpenMP.*

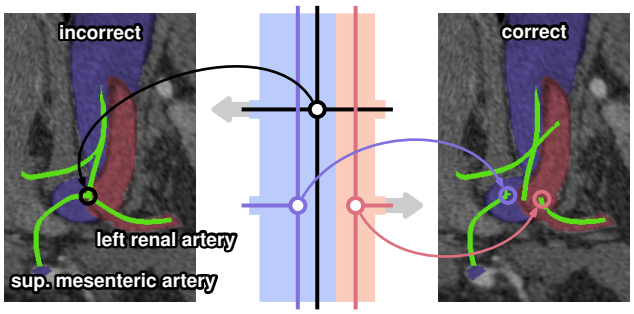

Figure 2: *Comparison between an incorrect (left) and correct (right) vessel tree for ADs. As pointed out, the left renal artery only connects to the true lumen (red) and therefore must branch from the true lumen centerline (red) of its parent and not from the combined true and false lumen centerline (black). Same for the superior mesenteric artery with the false lumen (blue).*

Simply extracting the skeleton of the combined true and false lumen masks does not lead to a suitable vessel tree, because branches connected to only one of the lumina would be erroneously connected to the center of the entire aorta and might contain parts of both lumina, as shown in the upper bifurcation of Fig. 2 and demonstrated in its left image. Alternatively, if we would consider both flow channels independently, we would not be able to extract matching contours of true and false lumen for the same cross-section. This is important for the measurement and comparison of both lumina.

To obtain a suitable vessel tree for ADs, we first compute the skeleton of the entire combined true and false lumen 3D segmentation mask, convert it to a graph representation, and only keep branches containing a dissection; all other branches are removed. We then compute the skeleton of the true lumen segmentation and keep branches consisting of true lumen only. This step is afterwards repeated for the false lumen. As illustrated in the lower bifurcation and the right image of Fig. 2, the centerlines of branches with a single lumen are not connected to the centerlines of branches with both lumina—the centerline of such a branch is defined as the centerline of the combined true and false lumen 3D segmentation masks. This ensures that individual flow channels are connected to their correct parent lumen.

Then, we smooth (binomial filter) the 3D points of each branch and represent them as an interpolating parametric curve $\mathbf{C}(u) = (x(u), y(u), z(u))^T$, with $\mathbf{C}(u) : \mathbb{R} \to \mathbb{R}^3$. To get an implicit surface of the aortic vasculature, we must create an affine mapping $M : \mathbb{R}^3 \to \mathbb{R}^3$, which transforms a point $\mathbf{P}$ from the embedding (world) space into the parameter—multiplanar reformation (MPR) or tangent [KGPS13]—space of the curve, $\hat{\mathbf{P}} = M(\mathbf{P})$. We define this mapping as rotation minimizing frame (RMF), the local orthonormal frame, which consists of an ordered triplet of vectors $U(u) = (\mathbf{r}(u), \mathbf{s}(u), \mathbf{t}(u))$, with $\mathbf{r}(u) \times \mathbf{s}(u) = \mathbf{t}(u)$ [WJZL08]. Any given point $\hat{\mathbf{P}} = (P_r, P_s, P_t) \in \mathbb{R}^3$ in the MPR space, which is defined by centerline point $\mathbf{C}_i$ and orthonormal frame $U_i = (\mathbf{r}_i, \mathbf{s}_i, \mathbf{t}_i)$, is mapped to world space by:

$$M : \mathbb{R}^3 \to \mathbb{R}^3, \tag{1}$$

$$M(\mathbf{P}) = \mathbf{U}_i^T \, (\mathbf{P} - \mathbf{C}_i) \ , \tag{2}$$

with its inverse mapping of

$$M^{-1} : \mathbb{R}^3 \to \mathbb{R}^3, \tag{3}$$

$$M^{-1}(\hat{\mathbf{P}}) = \mathbf{U}_i \hat{\mathbf{P}} + \mathbf{C}_i \ , \tag{4}$$

where the orthogonal matrix $\mathbf{U}_i$ has $\mathbf{r}_i, \mathbf{s}_i, \mathbf{t}_i$ as columns. Without a given orthonormal frame U_i, the mapping $M(\mathbf{P})$ from world to MPR space is not unique and could lead to multiple points [KGPS13].

We then sample the centerline $\mathbf{C}(u)$ at equidistant intervals d and obtain a discrete polyline with points $(\mathbf{C}_0, \ldots, \mathbf{C}_m)$. The 3D segmentation mask is then resampled in planes perpendicular to the centerline at these points, using their respective orthonormal frames. The sampling planes are defined by the orthogonal generating vectors $\mathbf{r}_i$ and $\mathbf{s}_i$. This results in a MPR volume for each branch. Since the true lumen usually rotates around the false lumen and changes its shape at the same time, we have to take samples close enough to capture these details. However, dense sampling could result in irregularities and non-smooth surfaces [KGPS13].

MPR resampling could lead to over-segmentation at bifurcations. Hong et al. [HLT12] reduce the effects of this problem by rejecting local contours when they exceed the size of the resampling plane. This approach cannot be used for dissections, because already small over-segmentations could include parts of another lumen and cause surface artifacts when reducing the number of EFD harmonics. A possible solution could be a direct segmentation of branches in MPR space, e.g. using the algorithm of Hahn et al. [HMH*20] and a correction similar to ellipse fitting [MZS*18]. As this is not the main focus of this work but rather an independent subproblem, we consider this future work and corrected such cases manually.

3.2. Contour Extraction

Once we created the MPR volume for each aortic branch, we extract the contours of each lumen, convert them to a chain code and calculate their EFDs. Compared to blood vessels with a single flow channel, we must take into account that multiple channels may start anywhere along the centerline of a branch, may reconnect multiple times, and may merge before the end. The blood enters proximally through the primary intimal tear into the false lumen and can re-enter downstream (distally) through the so-called re-entry tear into the true lumen. All other intermediate communications are called fenestrations [DMNNF16, AAB*19].

For each vessel branch, we extract the contours of all lumina slice-by-slice (in axial slices along the z-axis) in MPR space. Since we know the true and false lumen masks (see Fig. 3a), we extract their contours separately with the approach of Seo et al. [SCS*16]. As a result we get a list of pixels with their corresponding 2D positions and classes (straight-line, inner corner, outer corner, and inner-outer corner, see Fig. 3b). We then convert this list of absolute pixel positions to a 4-connected FCC (see Fig. 3c) by classifying the movements between successive points accordingly [KG82]. An 8-connected FCC (see Fig. 3d) can be obtained by ignoring pixels classified as inner corners. If not explicitly mentioned, we always use an 8-connected FCC.

Let T be the perimeter of the contour or Euclidean length of the 1D periodic signal of its corresponding FCC. If we move a point

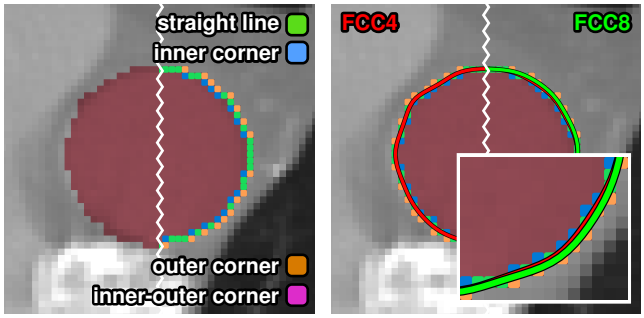

Figure 3: *Contour extraction. (a) shows the input image with the true lumen mask in red. (b) displays the result of the contour tracer. A reconstructed EFD contour with 10 harmonics is displayed from a 4-connected FCC in red (c) and an 8-connected FCC in green (d).*

p along the contour, starting from s, the elapsed time t denotes the (Euclidean) length of the contour from s to p. The Fourier series expansions in x- and y-direction is then given [KG82, LH87] as:

$$\begin{bmatrix} x(t) \\ y(t) \end{bmatrix} = \begin{bmatrix} A_0 \\ C_0 \end{bmatrix} + \sum_{n=1}^{N} \begin{bmatrix} a_n & b_n \\ c_n & d_n \end{bmatrix} \begin{bmatrix} \cos \frac{2\pi n t}{T} \\ \sin \frac{2\pi n t}{T} \end{bmatrix}, \tag{5}$$

where A_0 and C_0 are the DC components, N the number of harmonics, and a_n, b_n, c_n, d_n the Fourier coefficients. The Fourier coefficients are calculated as follows:

$$\begin{bmatrix} a_n & b_n \\ c_n & d_n \end{bmatrix} = \frac{2}{\omega^2 \Delta t_k} \sum_{k=1}^{K} \begin{bmatrix} \Delta x_k \\ \Delta y_k \end{bmatrix} [1 \; -1] \begin{bmatrix} \cos \omega t_k & \sin \omega t_k \\ \cos \omega t_{k-1} & \sin \omega t_{k-1} \end{bmatrix} \tag{6}$$

where $\omega = \frac{2\pi n}{T}$ and K is the number of chain code elements and Δx, Δy the x- and y-shift from the previous chain code element to the current one. Each movement of the FCC is associated with a length, where even directions have length one and odd directions have length $\sqrt{2}$, on a rectangular 2D lattice [KG82]. The length of a contour is defined as the sum of its movement lengths. The DC components A_0 and C_0 are computed as described below:

$$A_0 = \frac{1}{T} \sum_{k=1}^{K} \left[\frac{\Delta x_k}{2\Delta t_k} (t_k^2 - t_{k-1}^2) + \xi_k (t_k - t_{k-1}) \right], \tag{7}$$

$$C_0 = \frac{1}{T} \sum_{k=1}^{K} \left[\frac{\Delta y_k}{2\Delta t_k} (t_k^2 - t_{k-1}^2) + \delta_k (t_k - t_{k-1}) \right], \tag{8}$$

$$\xi_1 = 0, \text{ and } \xi_k = \sum_{j=1}^{k-1} \left(\Delta x_j - \frac{\Delta x_k}{\Delta t_k} \Delta t_j \right) \text{ for } k > 1, \tag{9}$$

$$\delta_1 = 0, \text{ and } \delta_k = \sum_{j=1}^{k-1} \left(\Delta y_j - \frac{\Delta y_k}{\Delta t_k} \Delta t_j \right) \text{ for } k > 1. \tag{10}$$

The final EFD of a contour consist of four Fourier coefficients per harmonic and two DC components corresponding to the center of the contour [KG82, NA02]. Several contours reconstructed with a different number of harmonics are shown in Fig. 4.

To avoid non-smooth or highly curved contours, which could be caused by noisy segmentations, the cross-sectional shape can be blended [KGPS13] or restricted [LWP*04, HLW*18] by another shape, e.g., an ellipse. These methods cannot be used for dissections because the shape of the lumina can change considerably longitudinally, which could lead to unwanted communication. With EFDs, we can control the smoothness of the cross-sectional shape by changing the number of harmonics for reconstruction. When decreasing the number of harmonics, we successively remove higher frequency shape information and keep only lower-level shape features.

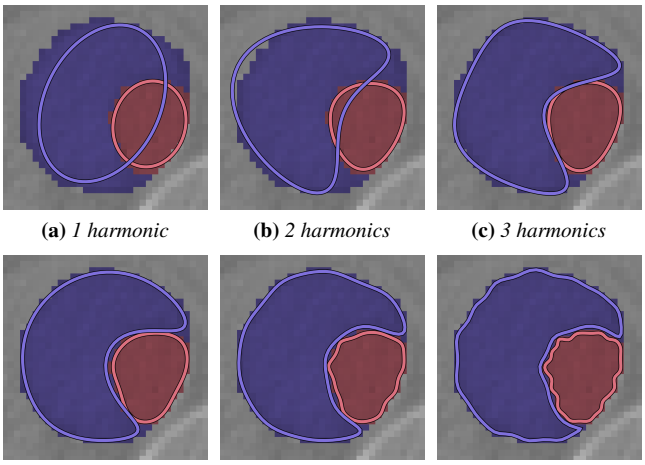

Figure 4: *EFDs of true and false lumen contours reconstructed with a different number of harmonics. Increasing the number of harmonics, successively adds higher frequency shape information. (Slight contour overlaps are caused by the line thickness selected for illustration purposes)*

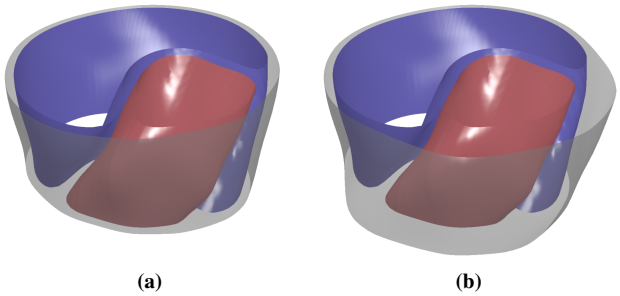

Figure 5: *Vessel walls with varying thickness. (a) shows a wall thickness of 1 mm for both lumina. (b) uses 4 mm for the true lumen and 1 mm for the false lumen to clearly depict their difference.*

Once we reconstructed the cross-sectional contours of the existing lumina, we compute the outer vessel wall (see Fig. 5). We dilate each lumen with a circular structuring element, where the radius is the desired wall thickness. The vessel wall contour is then the convex hull [And79] of both dilated lumina. Modeling the wall with a different thickness for the true and false lumen reflects the underlying anatomy of a dissection (see Fig. 5b). Since the false lumen delaminates the wall and reaches into the media aortic wall layer, the wall of the false lumen is thinner, making it more susceptible to high pressure. This is also important for CFD simulations and fluid-structure growth simulations of false lumen growth [Hum09].

3.3. Rendering

To render the entire vessel tree, we calculate three local distance volumes $\mathcal{L}(x,y,z)$ in MPR space for each branch, namely, one for the true lumen, one for the false lumen (if existing), and one for the outer vessel wall. Similar to Kretschmer et al. [KGPS13] we compute the Euclidean signed distance field for every contour polygon (z-slice, see Fig. 6a) of the true lumen, false lumen and the vessel wall, with a positive sign inside and a negative sign outside the contour (see Fig. 6b) [Qui30]. From this state on there is no conceptual difference between a flow channel and a branch.

Next, all local distance volumes are combined into a global distance volume $\mathcal{G}(x,y,z)$ that describes the distance to the iso-surface. We use separate distance volumes for the inner lumen surface (true and false lumen) and the outer vessel wall, but the approach is the same for both. By discretizing the global volume into a 3D lattice, we loop through each voxel and transform its index position $\overline{\mathbf{P}} = (u,v,w)$ into world or physical coordinate space $\mathbf{P} = (x,y,z)$. We model the implicit surface of a branch's lumen as the weighted sum of its cross-sectional contours (z-axis in MPR space). To calculate the contribution of a flow channel to point $\mathbf{P}$, we need to find the k-th centerline point that is closest to this point:

$$k = \underset{k\in\{0,\ldots,m\}}{\arg\min} \|\mathbf{C}_k - \mathbf{P}\|. \tag{11}$$

The implicit surface of a lumen is then described in MPR space as:

$$\Phi = \sum_{j=k-l}^{k+l} \mathcal{L}(\hat{P}_r, \hat{P}_s, j) B(\hat{P}_t), \tag{12}$$

where $\mathcal{L}(x,y,z)$ is the local MPR distance volume of the lumen, $B(t)$ is the PSP spline [LT11], $\hat{\mathbf{P}} = M(\mathbf{P})$ using orthonormal frame U_j, and l is the blending range, specified in number of centerline points. The PSP spline is defined as:

$$B(t) = B^m_{[a,b],\delta}(t) = H_m(\frac{b-t}{\delta}) - H_m(\frac{a-t}{\delta}), \tag{13}$$

with $a \leq b$, and $H_m(x)$ being the smooth unit step function [LGW06]. This ensures that cross-sections are smoothly blended within the interval $[a,b]$. Unless otherwise specified, we set $a = -d/2$, $b = d/2$, $m = 3$, and $\delta = d$ in our experiments, where $d = 3$ mm is the distance at which we MPR-resampled a centerline. The blending range is default to $l = 5$.

There are several reasons for limiting the blending of cross-sections to a specific range:

1. We do not need to partition the centerline into subsegments nor limit their MPR spaces with their bounding boxes [HLT12].
2. If we do not limit $B(t)$ [HLT12], this would lead to an undesired fusion of U-shaped blood vessels like the aortic arch. This is caused by the ambiguous mapping between world and MPR space, since a point could also be transformed to a small t-value (z-coordinate) at another centerline point.
3. If we used $B(k-j)$ [HLW*18] in Equation 12 instead of $B(t)$, branches would tend to extrude beyond their start- and end-points in our implementation. $B(k-j)$ was always 1 for points in the negative half-space of the start-point's cross-section plane, since their distance from the start-point is not considered [HLW*18, Eq. 6]. The same applies to points beyond the end-point, but in the positive half-space.

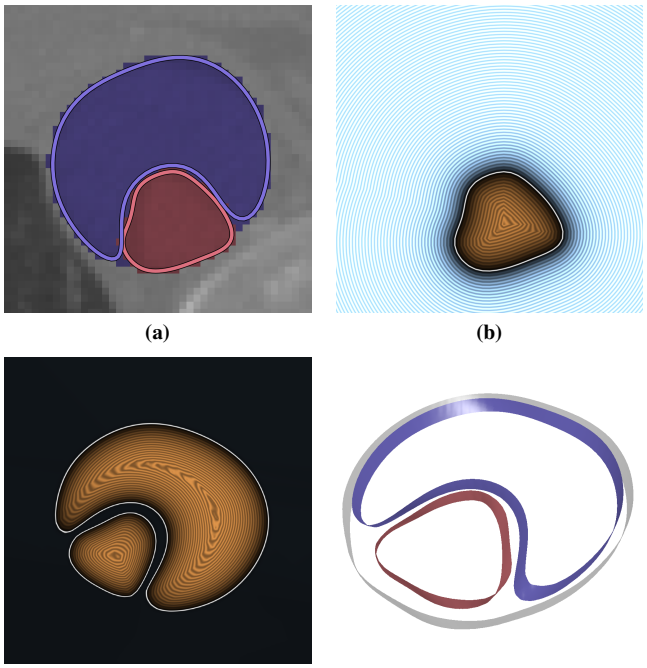

Figure 6: *Distance field computation. (a) shows the true and false lumen contours using six harmonics. The slight overlap of the contours is caused by the line thickness selected for illustration purposes. (b) displays the local distance field of the true lumen with inside being positive (orange) and outside being negative (blue). The global distance field of both lumina is shown in (c) and their corresponding geometry, including the wall, is presented in (d).*

Once we computed a lumen's implicit surface Φ at point $\overline{\mathbf{P}}$, we blend it with the global distance volume $\mathcal{G}(u,v,w)$ using the smooth maximum function [Li07]:

$$\max_{n,\gamma}(\mathcal{G},\Phi) = \frac{1}{2}(\mathcal{G} + \Phi + |\mathcal{G} - \Phi|_{n,\gamma}), \tag{14}$$

where $|\cdot|_{n,\gamma}$ is the smooth absolute function of degree n and blending range γ. Unless otherwise specified, $n = 2$ and $\gamma = 0.5$ in our experiments. All existing lumina are blended into a single distance volume and form one implicit surface. The same procedure is repeated for the vessel wall, leading to a separate wall surface. The final surfaces are then extracted with marching cubes [SEL12] using iso-value 0.5 (see Fig. 6c).

To render the lumina with different colors (see Fig. 6d), we classify each voxel of the final distance volume into true or false lumen. This is accomplished by passing the current lumen mask to the blending shader and writing it into the global classification volume whenever the local value Φ is larger than the global value (before blending with Equation 14) at the same position.

To demonstrate the possibilities of an implicit AD model, we created a phantom communication that should model the primary intimal tear of the dissection (see Fig. 7). It is spherical and included into the global lumen distance volume just before iso-surface extraction (recall Fig. 1, step 14).

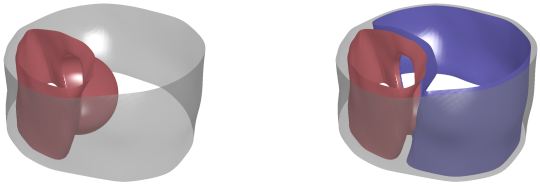

(a) (b)

Figure 7: *A spherical phantom communication. (a) shows only the true lumen with the communication attached to it. (b) displays how this leads to the communication between the two flow channels.*

4. Results

In this section we present several surfaces of ADs created with different EFDs. First, we show a phantom data set that demonstrates our approach on several true and false lumen arrangements as well as other vascular pathologies, such as stenoses. We then present two patients with different manifestations of ADs.

The **phantom data set** (see Fig. 8) resembles a CTA data set that consists of tissue and a straight tube in the middle. The tube is filled with contrast-enhanced blood and divided into two parts, separated by the high-grade stenosis (number 9) in the middle. Along the tube, we simulate several vascular pathologies and present for each a 3D visualization of the reconstructed surfaces and the corresponding 2D slice with the reconstructed contours, using 10 harmonics.

The upper part of the phantom data set is intended to show that our approach is able to deal with the high variability of lumen arrangements in aortic dissections. The main and most common lumen arrangements are, from top to center:

1. a small eccentric false lumen that gradually transforms into:
2. a large eccentric false lumen that rotates around the true lumen and successively occupies more cross-sectional area, until only
3. a crescent-shaped true lumen remains, which is very narrow. If the false lumen re-enters the true lumen, it may shrink again until
4. a small false lumen remains, which then disappears.

As the reconstructed surfaces show, our approach copes well with all these simulated cases, even when true and false lumen rotate around each other.

The purpose of the lower part of the phantom data set is to demonstrate the generalizability of our approach to vascular pathologies other than dissections. We present common forms of vascular stenoses that are usually examined by specific visualization techniques [MMV*13]. The pathologies are modeled with calcified or soft plaque and displayed in blue. The remaining vessel lumen is depicted in red. Typically, a vascular narrowing can be caused by:

5. a small eccentric calcification,
6. a concentric calcification that goes around the entire vessel wall,
7. a large eccentric calcification,
8. a large eccentric soft plaque, and
9. a high-grade concentric stenosis.

Number 6, the concentric calcification, presents a limitation of our approach, as the true lumen surface inside the false lumen is missing. With this exception, all types and forms of plaque are also properly

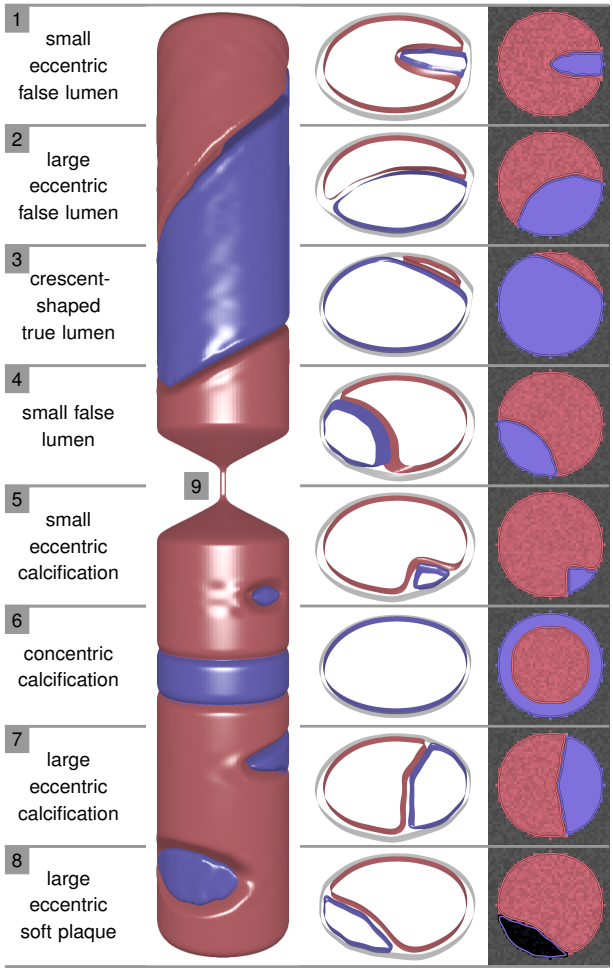

Figure 8: *A tubular phantom data set. The upper part (1-4) consists of common true and false lumen shapes encountered in the dissected aorta. Separated by the narrow stenosis (9), the lower part (5-8) shows usual shapes of plaque, either calcified or soft. Whereas the upper part demonstrates that our approach is suitable to represent aortic dissections, the lower part generalizes to other vascular pathologies, such as stenoses.*

managed by our approach. Thus, we can conclude that our approach is also suitable for visualizing cross-sections of vascular diseases other than aortic dissections.

Fig. 9 shows **Patient 1** with a TBAD starting in the descending thoracic aorta and leading to the abdominal aorta. The proximal entry tear is located in the descending thoracic aorta and the distal re-entry tear in the abdominal aorta. The left overview image shows the entire aorta created with 10 harmonics and a vessel wall thickness of 2 mm for the true lumen and 1 mm for the false lumen. Fig. 9a shows the aortic arch arteries from within the aorta. The true and false lumina are presented separately in Fig. 9b. By also visualizing the vessel wall, it becomes apparent how large the false lumen is compared to the true lumen. It is also clearly visible how the two lumina rotate around each other longitudinally. Fig. 9c demonstrates how branch centerlines are connected only to their corresponding parent lumen

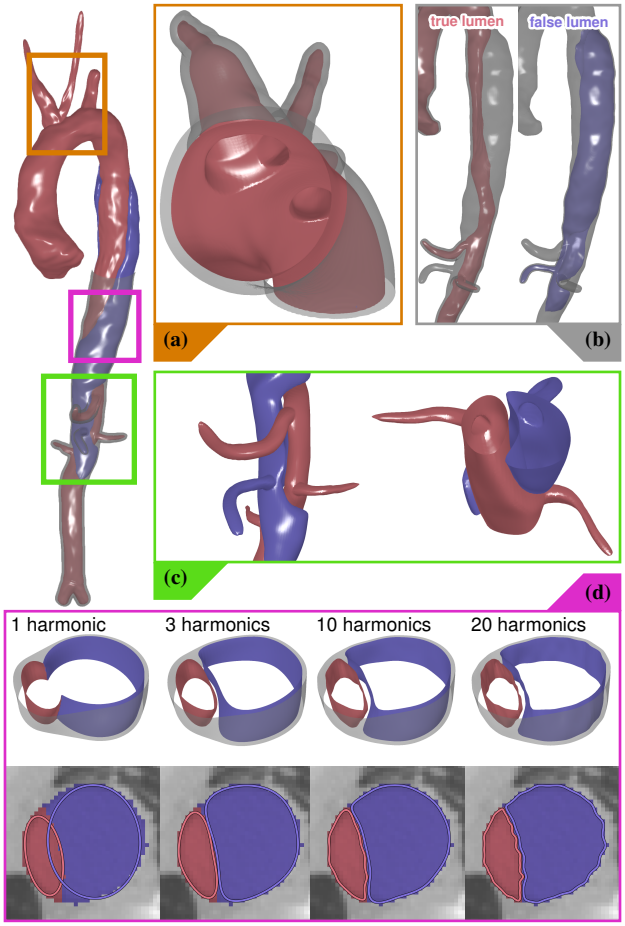

Figure 9: *Patient 1 with a TBAD from the descending thoracic aorta into the abdominal aorta. (a) shows how the aorta connects the arch arteries from the inside. (b) displays only the true lumen (left) and false lumen (right) with the vessel wall. (c) demonstrates how the branches are properly connected to their parent lumen. (d) displays the effect of different harmonics on the lumen and wall surfaces. When using only one harmonic, true and false lumen merge.*

(recall Fig. 2). The effect of the harmonics is presented in Fig. 9d. One harmonic causes the lumina to merge, whereas 20 harmonics add too much high frequency information. A good compromise between smoothness and accuracy is within 3-10 harmonics.

The aorta of **Patient 2** (see Fig. 10) comprises a long dissection that begins in the arch and extends far into the iliac arteries. The descending thoracic aorta is strongly dilated with a large false lumen and the branches in the abdominal aorta are properly connected to their parent lumen (see Fig. 10a). An abstraction of the dissected aorta is presented in Fig. 10b. Only one harmonic is used and the number of reconstructed contour points is reduced to four (left) and three (right). The overall shape of the aorta is still clearly visible, but the rotation of the false lumen around the true lumen becomes more apparent. A small dissection in one of the arch arteries is shown in Fig. 10c. The dissection in the iliac bifurcation is well preserved, as demonstrated with a cut through both iliac arteries (see Fig. 10d).

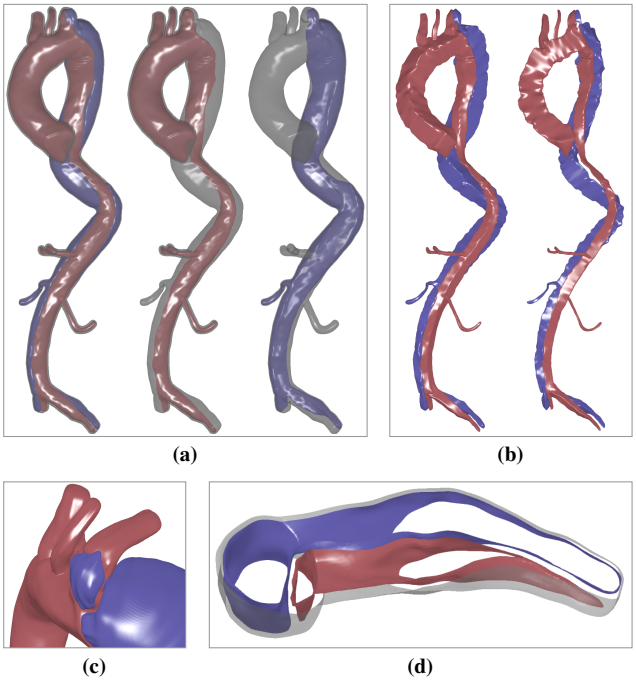

Figure 10: *Patient 2 with a TBAD from the end of the aortic arch far down into the iliac arteries. (a) shows both lumina (left), the true lumen (middle), and the false lumen (right). (b) presents an abstraction of the dissected aorta, created with only one harmonic and four (left) vs. three (right) contour points. (c) shows a zoom-in of a small dissection in one of the arch arteries. (d) shows a cut through the iliac arteries close to the iliac bifurcation to demonstrate how the dissection continues across branches.*

Table 1: *Performance of our approach in minutes and milliseconds. The steps with their numbers refer to the workflow (see Fig. 1).*

Step	Phantom	Patient 1	Patient 2
Construct vessel tree (2-4)	predefined	≈30 min	≈30 min
Create MPR volumes (5)	45.58 ms	53.18 ms	66.56 ms
Extract contours & EFDs (6-8)	21.85 ms	17.12 ms	26.98 ms
Reconstruct all contours (9-10)	12.99 ms	15.11 ms	22.33 ms
Compute local distance fields (11)	0.98 ms	4.58 ms	6.14 ms
Create lumen distance field (12)	0.52 ms	0.90 ms	0.90 ms
Create wall distance field (13)	0.02 ms	0.07 ms	0.07 ms
Extract lumen surface (15)	1181.50 ms	1884.98 ms	2547.39 ms
Extract wall surface (15)	655.51 ms	1424.87 ms	1647.34 ms
Number of lumen triangles	3 482 435	1 273 667	1 788 774
Number of wall triangles	2 640 860	1 296 410	1 616 108
MPR-resample distance	1 mm	3 mm	3 mm
Global distance volume size	512 × 512 × 768		

We determined the required **times** (see Table 1) of steps 2 to 15 of our workflow (recall Fig. 1). Measurements were taken on an Intel Core i7-8750H CPU @ 2.20 GHz with 32 GB RAM and an NVIDIA GeForce RTX 2070 with 8 GB VRAM and driver version 452.06. Our approach was implemented in C++ with Qt 5.12.1 for the user interface. We ported the marching cubes algorithm [SEL12] to OpenGL compute shaders and adapted it to support anisotropic

volumes, such as the global distance volume. Constructing the vessel trees (steps 2-4) for Patients 1 and 2 took the most time overall. This is due to finding appropriate threshold values for pruning spurious branches during skeletonization and subsequent semi-automatic assembly. Steps 5 to 8 are computed (CPU, OpenMP) only once for a data set and together require less than 100 ms. Steps 9 to 15 are computed whenever the number of harmonics is changed. To assess their performance, we averaged them over harmonics one to ten. Steps 9 and 10 (CPU, OpenMP) are below 30 ms, while steps 11 to 13 (GPU, OpenGL) are below 10 ms. Extracting the lumen and the outer vessel wall surfaces (step 15, GPU, OpenGL) required most time during rendering.

5. Evaluation

To evaluate our approach, we conducted a user study with eight participants in the form of a questionnaire (see Fig. 11). Participants included one clinical imaging technologist (P1) and five radiologists (P2-P6), two with less than 10 years of experience and the others with more than 15 years. Participants P7 and P8 had technical expertise (biomedical imaging and engineering), both with more than 10 years of experience. Before completing the questionnaire, the approach was explained and a demonstration video was shown.

All participants rated our approach *somewhat better* or *much better* than the current clinically used visualization tools such as volume rendering (**Q1**, 5-point Likert scale: 4.63 ± 0.52). The ability to display the true lumen, false lumen and outer vessel wall separately was universally rated as useful (**Q2**, 7-point Likert scale: 6.13 ± 0.64) because it facilitates the perception of the intertwined and overlapping flow channels commonly seen in aortic dissection.

All participants found our approach *suitable* (**Q3**, 7-point Likert scale) for the intended applications: quantifying aortic diameters or dimensions (6.25 ± 1.04), CFD computations (6.25 ± 1.04), 3D printing of models (5.88 ± 1.64), statistical analysis and modeling (6.38 ± 0.52), surgery planning (6.13 ± 0.35), and visualizing changes over time (6.25 ± 0.71).

Our approach was then evaluated for the same intended applications as in Q3, but with regard to importance in clinical applications (**Q4**, 7-point Likert scale). The quantification of aortic diameters or dimensions, surgery planning, and visualization of changes over time were rated *very important* (6.25 ± 1.04, 6.13 ± 1.46, (6.5 ± 0.76), respectively). CFD computations, 3D printing, and statistical modeling were considered as *neutral* to *moderately important* (4.63 ± 2.39, 4.63 ± 2.0, 4.88 ± 2.17, respectively).

The next question examined the importance of our method for research and future development (**Q5**, 7-point Likert scale). In all but four fields, the ratings were more positive than Q4, clinical applications, with scores of *moderately important* or higher: quantifying aortic diameters or dimensions (6.0 ± 0.76), CFD computations (6.38 ± 0.52), 3D printing of models (5.63 ± 1.6), statistical analysis and modeling (6.38 ± 0.52), surgery planning (5.13 ± 2.1), and visualizing changes over time (6.13 ± 1.73).

Regarding the limitation of displaying circumferential cross-sections (**Q6**, 7-point Likert scale), six participants rated at least *slightly acceptable* (5.13 ± 1.55), one participant was *neutral*, and another rated *unacceptable*.

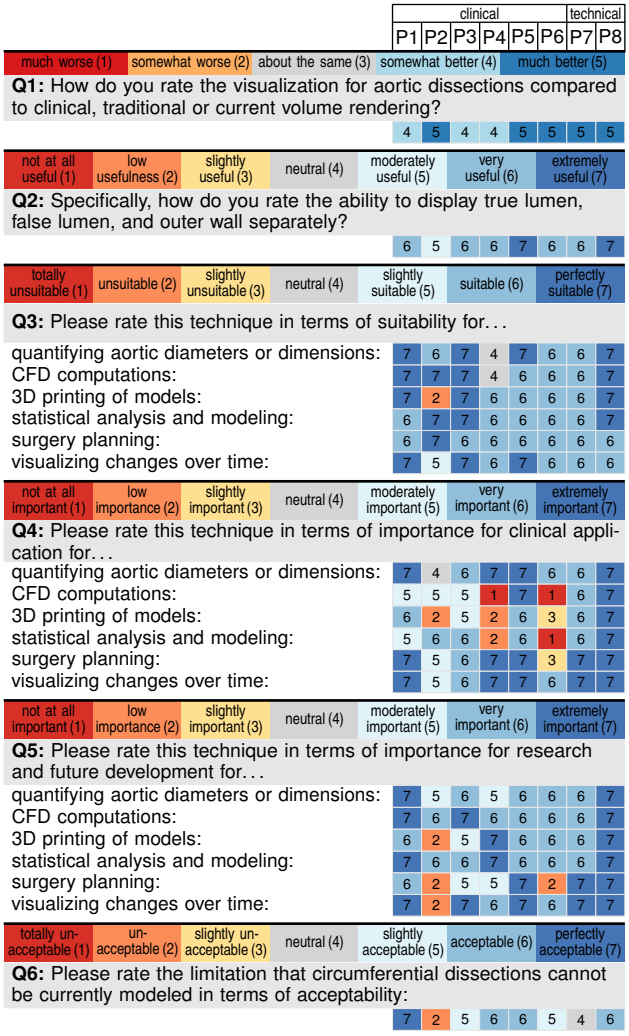

Figure 11: *Evaluation of our approach.*

We also investigated the preferred number **number of harmonics**. To this end, we presented the participants 2D contours, analogously to Fig. 4, for harmonics 1-10, 12, 16, and 20. Participants chose 6, 7, 8, 9 (3×), 12, 20, with an average of 10.

Regarding **other applications** of our visualization, participants reported: patient communication, patient education, planning of complex surgical cases, and navigation during surgery. Other comments included patient risk classification, medical devices, aortic atlas, and left ventricle segmentation from cardiac magnetic resonance imaging as well as functional analysis. One participant explicitly mentioned, *this work is clearly a stepping stone to other analyses*.

6. Discussion and Limitations

There exist various alternative models for representing a contour by either a parametric or an implicit function. Cubic Hermite splines like Catmull-Rom splines as used by Kretschmer et al. [KGPS13] can be constructed efficiently without solving a linear system, and also the evaluation at a parameter is fairly inexpensive. The ap-

proximation of a signed distance field with implicit functions does not need or depend on a parametrization. A popular choice for multivariate interpolation are radial basis functions as used, e.g., in [LWP*04, HLW*18, EWD*18]. Interpolation with implicit functions, requires samples not only on the contour but also inside and outside. The latter off-contour samples are ideally taken from offset curves, which are unfortunately unknown. In practice they are generated from small offsets in normal direction. The fitting depends on the choice of samples and can give unacceptable results like topology changes for isocurves. Such effects cannot be effectively controlled. This lack of robustness makes them a questionable choice for medical applications. An alternative are piecewise implicit functions like PA splines [LT09, HLT12], which can be constructed directly from closed polylines. However, they may trade smoothness for interpolation, and their evaluation may be too expensive.

An alternative are Poisson surface reconstruction (PSR) methods, that generate an implicit surface from an unstructured point cloud. These methods are efficient and robust, possibly include regularization to enforce smooth/fair surfaces, which makes them often the method of choice for generic implicit surface reconstruction problems. We do not use PSR, because we need to solve a very specific problem: We already have a model assumption on the geometry of the vessel surface from the centerlines and an appropriate "structured" sampling. A PSR could not use this information. Moreover, the vessel model defines the topology of the reconstruction. The standard PSR methods cannot provide any guarantees on topology. There is recent work on topology priors [BGGSSG20], but it remains unclear whether our setup could benefit from this more complex approach. Finally, our solution fits the purpose, is considerably simpler and more efficient: PSR is a global method (we blend slices) and requires either the solution of a large sparse linear system or diagonalizing the linear operator by changing to a spectral basis.

The representation of contours in the Fourier domain as used in this paper provides a number of advantages: Firstly, the construction is efficient for both, computing the Fourier coefficients and reconstructing polylines from harmonics. Secondly, it inherently provides an analysis of the shape as different levels of geometric detail are encoded in different frequency bands: Reconstruction from only the first harmonics provide a very smooth but coarse approximation. The reconstruction becomes more accurate when adding more harmonics, as finer geometric detail is encoded in higher frequencies. Note that with better approximation and fine details the reconstructed contours appear less smooth (see Fig. 4). A potential drawback of harmonic analysis is the lack of interpolation unless all harmonics are used for reconstruction. We tend to see this rather as an advantage than as disadvantage due to smoother reconstruction and the fact that the approximation appears robust and generally sufficient for our purpose.

To avoid misalignment of successive cross-sections, the sampling should not be too sparse, since the lumina tend to twist around each other and change their cross-sectional shape. For this reason, we resampled the vessel centerlines at regular intervals with $d = 3$ mm. An alternative would be spline-based interpolation, defined by the cross-sections' centers of gravity [KGPS13].

The surface representation with EFDs and subsequent implicit surface rendering also allows the user to reduce the discretization artifacts of contour lines. This is done by choosing an appropriate number of harmonics for the given application. One relevant example is the geometric model generation as an input for CFD simulations, where the user will rely on a smooth yet accurate surface representation. If fluid-structure interaction simulations are performed, the possibility to extract a wall model is especially relevant. The possibility to incorporate varying wall thickness for true and false lumen wall respectively can be used to increase the accuracy of the resulting model, as supported by Q2.

Another interesting application of the rendered surface model could be to investigate the effects of small scale spatial inaccuracies as they are increasingly present with the inclusion of higher harmonics. These effects could be studied with regard to clinical measurements as well as subsequent CFD simulations based on the respective surface representation.

Our approach has two **limitations**. The first limitation deals with merging of true and false lumen when the number of harmonics is too small, i.e., less than three in our experiments (see Fig. 4 and Fig. 9d). A potential solution could use the local distance fields to correct the overlapping regions. The second limitation concerns the rare event of circumferential dissections (see Fig. 8 number 6). The reason for this is modeling the lumina with a single contour. Therefore, the distance field of the missing true lumen is overwritten inside the false lumen during smooth maximum blending. A possible solution would model lumina with two contours, an inner and an outer one, and track both [SCS*16]. However, this was considered acceptable in its current state (Q6).

7. Conclusion and Future Work

We presented an approach that creates high-quality surface representations for ADs. By using EFDs as cross-section representation, we can control the smoothness of the generated surface interactively and adapt it to application specific requirements. We demonstrated our approach on two different patients with ADs, and showed that the dissection smoothly continuous across vessel branches. By rendering the outer vessel wall, the degree of false lumen dilatation becomes quickly apparent. To this end, we showed an abstracted representation of an AD, by reducing the number of reconstructed contour points and the harmonics.

As we mentioned in the introduction, one application of the presented EFD-based surface representation is to obtain reliable measurements of ADs that are of clinical interest, such as maximum aortic diameter, true and false lumen volume or cross-sectional area, connectivity of branches to true and false lumen and others. With our approach, all features can be automatically extracted along the whole aorta, as long as a segmentation mask exists. While creating such segmentation masks manually is time-consuming, we are currently exploring data-driven approaches to obtain them automatically or semi-automatically with the help of machine learning algorithms, as surveyed in the work of Pepe et al. [PLRP*20].

Acknowledgments

The medical data sets were acquired at Stanford School of Medicine, approved by the institutional review board (IRB#41660). We thank Dietrich Trepnau for his support during his Master's thesis [Tre19].

References

[AAB*19] ALLEN B. D., AOUAD P. J., BURRIS N. S., RAHSEPAR A. A., JARVIS K. B., FRANCOIS C. J., BARKER A. J., MALAISRIE S. C., CARR J. C., COLLINS J. D., MARKL M.: Detection and hemodynamic evaluation of flap fenestrations in type B aortic dissection with 4D flow MRI: Comparison with conventional MRI and CT angiography. *Radiology: Cardiothoracic Imaging 1* (2019), e180009. doi:10.1148/ryct.2019180009. 4

[AGL*20] ABDELLAH M., GUERRERO N. R., LAPERE S., COGGAN J. S., KELLER D., COSTE B., DAGAR S., COURCOL J.-D., MARKRAMAN H., SCHÜRMANN F.: Interactive visualization and analysis of morphological skeletons of brain vasculature networks with VessMorphoVis. *Bioinformatics 36*, 1 (2020), i534–i541. doi:10.1093/bioinformatics/btaa461. 3

[AMZ99] AGUADO A. S., MONTIEL E., ZALUSKA E.: Modeling generalized cylinders via Fourier morphing. *ACM Transactions on Graphics 18*, 4 (1999), 293–315. doi:10.1145/337680.337683. 2, 3

[And79] ANDREW A. M.: Another efficient algorithm for convex hulls in two dimensions. *Information Processing Letters 9*, 5 (1979), 216–219. doi:10.1016/0020-0190(79)90072-3. 5

[BGGSSG20] BRÜEL-GABRIELSSON R., GANAPATHI-SUBRAMANIAN V., SKRABA P., GUIBAS L. J.: Topology-aware surface reconstruction for point clouds. *Computer Graphics Forum 39*, 5 (2020), 197–207. doi:DOI:10.1111/cgf.14079. 10

[Bri99] BRIBIESCA E.: A new chain code. *Pattern Recognition 32*, 2 (1999), 235–251. doi:10.1016/S0031-3203(98)00132-0. 2

[Bri00] BRIBIESCA E.: A chain code for representing 3D curves. *Pattern Recognition 33*, 5 (2000), 755–765. doi:10.1016/S0031-3203(99)00093-X. 2

[Bri04] BRIBIESCA E.: 3D-curve representation by means of a binary chain code. *Mathematical and Computer Modelling 40*, 3–4 (2004), 285–295. doi:10.1016/j.mcm.2004.01.003. 2

[Bri08] BRIBIESCA E.: A method for representing 3D tree objects using chain coding. *Journal of Visual Communication and Image Representation 19*, 3 (2008), 184–198. doi:10.1016/j.jvcir.2008.01.001. 2

[BVS*20] BÄUMLER K., VEDULA V., SAILER A. M., SEO J., CHIU P., MISTELBAUER G., CHAN F. P., FISCHBEIN M. P., MARSDEN A. L., FLEISCHMANN D.: Fluid-structure interaction simulations of patient-specific aortic dissection. *Biomechanics and Modeling in Mechanobiology 19* (2020), 1607–1628. doi:10.1007/s10237-020-01294-8. 1, 3

[CM16] CHIU P., MILLER D. C.: Evolution of surgical therapy for stanford acute type A aortic dissection. *Annals of Cardiothoracic Surgery 5*, 4 (2016), 275–295. doi:10.21037/acs.2016.05.05. 1

[CO17] CHITWOOD D. H., OTONI W. C.: Morphometric analysis of Passiflora leaves: the relationship between landmarks of the vasculature and elliptical Fourier descriptors of the blade. *GigaScience 6*, 1 (2017), 1–13. doi:10.1093/gigascience/giw008. 2

[DMNNF16] DILLON-MURPHY D., NOORANI A., NORDSLETTEN D., FIGUEROA C. A.: Multi-modality image-based computational analysis of haemodynamics in aortic dissection. *Biomechanics and Modeling in Mechanobiology 15* (2016), 857–876. doi:10.1007/s10237-015-0729-2. 4

[EWD*18] EIGEN K., WELS M., DOHLE D.-S., SUEHLING M., MAIER A.: Geometric modeling of the aortic inner and outer vessel wall from CTA for aortic dissection analysis. In *Proceedings of SPIE Medical Imaging: Image-Guided Procedures, Robotic Interventions, and Modeling* (2018), vol. 10576, pp. 1–8. doi:10.1117/12.2293096. 3, 10

[Fre61] FREEMAN H.: On the encoding of arbitrary geometric configurations. *IRE Transactions on Electronic Computers EC-10*, 2 (1961), 260–268. doi:10.1109/TEC.1961.5219197. 2

[Fre74] FREEMAN H.: Computer processing of line-drawing images. *ACM Computing Surveys 6*, 1 (1974), 57–97. doi:10.1145/356625.356627. 2

[GBC*13] GOURMEL O., BARTHE L., CANI M.-P., WYVILL B., BERNHARDT A., PAULIN M., GRASBERGER H.: A gradient-based implicit blend. *ACM Transactions on Graphics 32*, 2 (2013), 12:1–12:12. doi:10.1145/2451236.2451238. 3

[HBB*10] HIRATZKA L. F., BAKRIS G. L., BECKMAN J. A., BERSIN R. M., CARR V. F., CASEY JR D. E., EAGLE K. A., HERMANN L. K., ISSELBACHER E. M., KAZEROONI E. A., KOUCHOUKOS N. T., LYTLE B. W., MILEWICZ D. M., REICH D. L., SEN S., SHINN J. A., SVENSSON L. G., WILLIAMS D. M.: 2010 ACCF/AHA/AATS/ACR/ASA/SCA/SCAI/SIR/STS/SVM guidelines for the diagnosis and management of patients with thoracic aortic disease. *Circulation 121*, 13 (2010), 266–369. doi:10.1161/CIR.0b013e3181d4739e. 1

[HLT12] HONG Q., LI Q., TIAN J.: Implicit reconstruction of vasculatures using bivariate piecewise algebraic splines. *IEEE Transactions on Medical Imaging 31*, 3 (2012), 543–553. doi:10.1109/TMI.2011.2172455. 3, 4, 6, 10

[HLW*18] HONG Q., LI Q., WANG B., LIU K., LIN F., LIN J., CHENG X., ZHANG Z., ZENG M.: Accurate geometry modeling of vasculatures using implicit fitting with 2D radial basis functions. *Computer Aided Geometric Design 62* (2018), 206–216. doi:10.1016/j.cagd.2018.03.006. 2, 3, 5, 6, 10

[HLW*20] HONG Q., LI Q., WANG B., TIAN J., XU F., LIU K., CHENG X.: High-quality vascular modeling and modification with implicit extrusion surfaces for blood flow computations. *Computer Methods and Programs in Biomedicine 196* (2020), 105598. doi:10.1016/j.cmpb.2020.105598. 3

[HMH*20] HAHN L. D., MISTELBAUER G., HIGASHIGAITO K., KOCI M., WILLEMINK M. J., SAILER A. M., FISCHBEIN M., FLEISCHMANN D.: CT-based true- and false-lumen segmentation in type B aortic dissection using machine learning. *Radiology: Cardiothoracic Imaging 2*, 3 (2020). doi:https://doi.org/10.1148/ryct.2020190179. 4

[HPSP01] HAHN H. K., PREIM B., SELLE D., PEITGEN H. O.: Visualization and interaction techniques for the exploration of vascular structures. In *Proceedings of Visualization* (2001), pp. 395–402. doi:10.1109/VISUAL.2001.964538. 2, 3

[Hum09] HUMPHREY J. D.: Coupling hemodynamics with vascular wall mechanics and mechanobiology to understand intracranial aneurysms. *International Journal of Computational Fluid Dynamics 23*, 8 (2009), 569–581. doi:10.1080/10618560902832712. 5

[IEUH15] IWATA H., EBANA K., UGA Y., HAYASHI T.: Genomic prediction of biological shape: Elliptic Fourier analysis and kernel partial least squares (PLS) regression applied to grain shape prediction in rice (Oryza sativa L.). *PLoS ONE 10*, 3 (2015), e0120610. doi:10.1371/journal.pone.0120610. 2

[IU02] IWATA H., UKAI Y.: SHAPE: A computer program package for quantitative evaluation of biological shapes based on elliptic Fourier descriptors. *Journal of Heredity 93*, 5 (2002), 384–385. doi:10.1093/jhered/93.5.384. 2

[JR07] JEONG Y., RADKE R. J.: Reslicing axially sampled 3D shapes using elliptic Fourier descriptors. *Medical Image Analysis 11*, 2 (2007), 197–206. doi:10.1016/j.media.2006.12.003. 2

[KG82] KUHL F. P., GIARDINA C. R.: Elliptic Fourier features of a closed contour. *Computer Graphics and Image Processing 18*, 3 (1982), 236–258. doi:10.1016/0146-664X(82)90034-X. 2, 4, 5

[KGPS13] KRETSCHMER J., GODENSCHWAGER C., PREIM B., STAMMINGER M.: Interactive patient-specific vascular modeling with sweep surfaces. *IEEE Transactions on Visualization and Computer Graphics 19*, 12 (2013), 2828–2837. doi:10.1109/TVCG.2013.169. 2, 3, 4, 5, 6, 9, 10

[LGW06] LI Q., GRIFFITHS J. G., WARD J.: Constructive implicit fitting. *Computer Aided Geometric Design 23*, 1 (2006), 17–44. doi:10.1016/j.cagd.2005.04.011. 3, 6

[LH87] LIN C.-S., HWANG C.-L.: New forms of shape invariants from

elliptic fourier descriptors. *Pattern Recognition 20*, 5 (1987), 535–545. doi:10.1016/0031-3203(87)90080-X. 2, 5

[Li07] LI Q.: Smooth piecewise polynomial blending operations for implicit shapes. *Computer Graphics Forum 26*, 2 (2007), 157–171. doi:10.1111/j.1467-8659.2007.01011.x. 3, 6

[LT09] LI Q., TIAN J.: 2D piecewise algebraic splines for implicit modeling. *ACM Transactions on Graphics 28*, 2 (2009), 13:1–13:19. doi:10.1145/1516522.1516524. 3, 10

[LT11] LI Q., TIAN J.: Partial shape-preserving splines. *Computer-Aided Design 43*, 4 (2011), 394–409. doi:10.1016/j.cad.2011.01.007. 3, 6

[LWP*04] LI Q., WILLS D., PHILLIPS R., VIANT W. J., GRIFFITHS J. G., WARD J.: Implicit fitting using radial basis functions with ellipsoid constraint. *Computer Graphics Forum 23*, 1 (2004), 55–69. doi:10.1111/j.1467-8659.2004.00005.x. 3, 5, 10

[LŽ05] LIU Y. K., ŽALIK B.: An efficient chain code with Huffman coding. *Pattern Recognition 38*, 4 (2005), 553–557. doi:10.1016/j.patcog.2004.08.017. 2

[MHM*16] MUSSA F. F., HORTON J. D., MORIDZADEH R., NICHOLSON J., TRIMARCHI S., EAGLE K. A.: Acute aortic dissection and intramural hematoma: A systematic review. *JAMA 316*, 7 (2016), 754–763. doi:10.1001/jama.2016.10026. 1

[MMV*13] MISTELBAUER G., MORAR A., VARCHOLA A., SCHERNTHANER R., BACLIJA I., KÖCHL A., KANITSAR A., BRUCKNER S., GRÖLLER M. E.: Vessel visualization using curvicircular feature aggregation. *Computer Graphics Forum 32*, 3 (2013), 231–240. doi:10.1111/cgf.12110. 7

[MPJ12] MEBATSION H. K., PALIWAL J., JAYAS D. S.: Evaluation of variations in the shape of grain types using principal components analysis of the elliptic Fourier descriptors. *Computers and Electronics in Agriculture 80* (2012), 63–70. doi:10.1016/j.compag.2011.10.016. 2

[MSS*16] MISTELBAUER G., SCHMIDT J., SAILER A.-M., BÄUMLER K., WALTERS S., FLEISCHMANN D.: Aortic dissection maps: Comprehensive visualization of aortic dissections for risk assessment. In *Proceedings of Eurographics Workshop on Visual Computing for Biology and Medicine* (2016), pp. 143–152. doi:10.2312/vcbm.20161282. 3

[MZS*18] MISTELBAUER G., ZETTWITZ M., SCHERNTHANER R., FLEISCHMANN D., TEUTSCH C., PREIM B.: Visual assessment of vascular torsion using ellipse fitting. In *Proceedings of Eurographics Workshop on Visual Computing for Biology and Medicine* (2018), Puig Puig A., Schultz T., Vilanova A., Hotz I., Kozlikova B., Vázquez P.-P., (Eds.), pp. 129–133. doi:10.2312/vcbm.20181238. 4

[NA02] NIXON M. S., AGUADO A. S.: *Feature Extraction and Image Processing*, 1st ed. Newnes, 2002. ISBN: 0-7506-5078-8. 2, 5

[OP05] OELTZE S., PREIM B.: Visualization of vasculature with convolution surfaces: Method, validation and evaluation. *IEEE Transactions on Medical Imaging 24*, 4 (2005), 540–548. doi:10.1109/TMI.2004.843196. 2

[PLRP*20] PEPE A., LI J., ROLF-PISSARCZYK M., GSAXNER C., CHEN X., HOLZAPFEL G. A., EGGER J.: Detection, segmentation, simulation and visualization of aortic dissections: A review. *Medical Image Analysis 65*, 101773 (2020), 1–16. doi:10.1016/j.media.2020.101773. 10

[QLCH20] QI Q., LI Q.-D., CHENG Y., HONG Q.-Q.: Skeleton marching-based parallel vascular geometry reconstruction using implicit functions. *International Journal of Automation and Computing 17*, 1 (2020), 30–43. doi:10.1007/s11633-019-1189-4. 3

[Qui30] QUILEZ I.: 2D distance functions. https://www.iquilezles.org/www/index.htm, visited on 2020-11-30. 6

[SCBRD07] SÁNCHEZ-CRUZ H., BRIBIESCA E., RODRÍGUEZ-DAGNINO R. M.: Efficiency of chain codes to represent binary objects. *Pattern Recognition 40*, 6 (2007), 1660–1674. doi:10.1016/j.patcog.2006.10.013. 2

[SCLVC14] SÁNCHEZ-CRUZ H., LÓPEZ-VALDEZ H. H., CUEVAS F. J.: A new relative chain code in 3D. *Pattern Recognition 47*, 2 (2014), 769–788. doi:10.1016/j.patcog.2013.08.010. 2

[SCS*16] SEO J., CHAE S., SHIM J., KIM D., CHEONG C., HAN T.-D.: Fast contour-tracing algorithm based on a pixel-following method for image sensors. *Sensors 16*, 3 (2016), 1–27. doi:10.3390/s16030353. 4, 10

[SEL12] SMISTAD E., ELSTER A. C., LINDSETH F.: Real-time surface extraction and visualization of medical images using OpenCL and GPUs. In *Proceedings of Norsk informatikkonferanse* (2012), pp. 141–152. 6, 8

[SIK*17] SATO H., ITO T., KURODA Y., UCHIYAMA H., WATANABE T., YASUDA N., NAKAZAWA J., HARADA R., KAWAHARADA N.: New predictor of aortic enlargement in uncomplicated type B aortic dissection based on elliptic Fourier analysis. *European Journal of Cardio-Thoracic Surgery 52*, 6 (2017), 1118–1124. doi:10.1093/ejcts/ezx191. 2

[SKNŽ20] STRNAD D., KOHEK Š., NERAT A., ŽALIK B.: Efficient representation of geometric tree models with level-of-detail using compressed 3D chain code. *IEEE Transactions on Visualization and Computer Graphics 26*, 11 (2020), 3177–3188. doi:10.1109/TVCG.2019.2924430. 2

[SOB*07] SCHUMANN C., OELTZE S., BADE R., PREIM B., PEITGEN H.-O.: Model-free surface visualization of vascular trees. In *Proceedings of Eurographics/IEEE-VGTC Symposium on Visualization* (2007), pp. 283–290. doi:10.2312/VisSym/EuroVis07/283-290. 2, 3

[SvKN*17] SAILER A. M., VAN KUIJK S. M. J., NELEMANS P., CHIN A. S., KINO A., HUININGA M., SCHMIDT J., MISTELBAUER G., BÄUMLER K., CHIU P., FISCHBEIN M. P., DAKE M. D., MILLER D. C., SCHURINK G. W. H., FLEISCHMANN D.: Computed tomography imaging features in acute uncomplicated Stanford type-B aortic dissection predict late adverse events. *Circulation CardioVascular Imaging 10*, 4 (2017). doi:10.1161/CIRCIMAGING.116.005709. 1

[Tre19] TREPNAU D.: *Aortic Dissection Cross-section Model*. Master's thesis, Department of Simulation and Graphics, Otto-von-Guericke University Magdeburg, Magdeburg, Germany, 2019. 10

[WFEG*20] WUNDRAM M., FALK V., EULERT-GREHN J.-J., HERBST H., THURAU J., LEIDEL B. A., GÖNCZ E., BAUER W., HABAZETTL H., KURZ S. D.: Incidence of acute type A aortic dissection in emergency departments. *Scientific Reports 10*, 7434 (2020). doi:10.1038/s41598-020-64299-4. 1

[WJZL08] WANG W., JÜTTLER B., ZHENG D., LIU Y.: Computation of rotation minimizing frames. *ACM Transactions on Graphics 27*, 1 (2008), 2:1–2:18. doi:10.1145/1330511.1330513. 4

[WWL*10] WU J., WEI M., LI Y., XIN MA AND F. J., HU Q.: Scale-adaptive surface modeling of vascular structures. *BioMedical Engineering OnLine 9*, 75 (2010), 1–16. doi:10.1186/1475-925X-9-75. 2, 3

[YKR08] YANG M., KPALMA K., RONSIN J.: A survey of shape feature extraction techniques. In *Pattern Recognition Techniques, Technology and Applications*, Yin P.-Y., (Ed.). IntechOpen, 2008, pp. 43–90. doi:10.5772/6237. 2

[ZR72] ZAHN C. T., ROSKIES R. Z.: Fourier descriptors for plane closed curves. *IEEE Transactions on Computers C-21*, 3 (1972), 269–281. doi:10.1109/TC.1972.5008949. 2